Nonvolatile Electrically Reconfigurable Integrated Photonic Switch Enabled by a Silicon PIN Diode Heater

Jiajiu Zheng,* Zhuoran Fang, Changming Wu, Shifeng Zhu, Peipeng Xu, Jonathan K. Doylend, Sanchit Deshmukh, Eric Pop, Scott Dunham, Mo Li, and Arka Majumdar*

Reconfigurability of photonic integrated circuits (PICs) has become increasingly important due to the growing demands for electronic–photonic systems on a chip driven by emerging applications, including neuromorphic computing, quantum information, and microwave photonics. Success in these fields usually requires highly scalable photonic switching units as essential building blocks. Current photonic switches, however, mainly rely on materials with weak, volatile thermo-optic or electro-optic modulation effects, resulting in large footprints and high energy consumption. As a promising alternative, chalcogenide phase-change materials (PCMs) exhibit strong optical modulation in a static, self-holding fashion, but the scalability of present PCM-integrated photonic applications is still limited by the poor optical or electrical actuation approaches. Here, with phase transitions actuated by in situ silicon PIN diode heaters, scalable nonvolatile electrically reconfigurable photonic switches using PCM-clad silicon waveguides and microring resonators are demonstrated. As a result, intrinsically compact and energy-efficient switching units operated with low driving voltages, near-zero additional loss, and reversible switching with high endurance are obtained in a complementary metal-oxide-semiconductor (CMOS)-compatible process. This work can potentially enable very large-scale CMOS-integrated programmable electronic–photonic systems such as optical neural networks and general-purpose integrated photonic processors.

Advances in PICs, in particular, silicon photonics, have enabled chip-scale integration of photonic systems with electronic circuits.[1] As Moore's Law slows down and the electronic von Neumann bottleneck (i.e., the information traffic jam between the memory and processor) gets worse, these photonic systems are becoming more and more attractive by offering broad bandwidth with energy-efficient information transport, processing, and storage.[2] They are especially desirable when it comes to emerging applications such as neuromorphic computing,[3] quantum information,[4,5] and microwave photonics,[6,7] most of which require general-purpose programmable PICs.[8–10] Inspired by the field-programmable gate arrays (FPGAs) in electronics, such generic PICs or optical FPGAs usually consist of a mesh of photonic switches that can be reconfigured on demand to the bar, cross, or coupler states[8–10] to provide different functionalities, including universal linear transformation.[9,10] Current switches in these photonic systems, however, primarily rely on thermo-optic[11] or electro-optic[12,13] modulation effects that are weak and volatile. The resulting large footprint and constant high energy consumption thus restrict the scalability of such optical FPGAs.

Chalcogenide PCMs such as $Ge_2Sb_2Te_5$ (GST) have recently raised considerable interest because of their exceptional nonvolatile reconfigurability.[14,15] Upon structural phase transitions between the covalent-bonded amorphous state and the resonant-bonded crystalline state, PCMs exhibit substantial contrast in electrical resistivity[16] and optical constants (usually $\Delta n > 1$) over a broad spectral range.[14,15,17] Once switched, the resulting state can be retained for more than ten years under ambient conditions in no need of any external power supply.[16,18] Additionally, PCMs

J. Zheng, Z. Fang, C. Wu, Prof. S. Dunham, Prof. M. Li, Prof. A. Majumdar
Department of Electrical and Computer Engineering
University of Washington
Seattle, WA 98195, USA
E-mail: jjzno1@uw.edu; arka@uw.edu
S. Zhu, Prof. S. Dunham, Prof. M. Li, Prof. A. Majumdar
Department of Physics
University of Washington
Seattle, WA 98195, USA

The ORCID identification number(s) for the author(s) of this article can be found under https://doi.org/10.1002/adma.202001218.

Prof. P. Xu
Laboratory of Infrared Materials and Devices
Advanced Technology Research Institute
Ningbo University
Ningbo 315211, China
Dr. J. K. Doylend
Silicon Photonic Products Division
Intel Corporation
Santa Clara, CA 95054, USA
Dr. S. Deshmukh, Prof. E. Pop
Department of Electrical Engineering
Stanford University
Stanford, CA 94305, USA

**ADVANCED
SCIENCE NEWS**

www.advancedsciencenews.com

**ADVANCED
MATERIALS**

www.advmat.de

can be reversibly switched by low-energy[15,19–21] optical or electrical pulses on a sub-nanosecond timescale[22–24] with potentially long endurance up to 10^{15} cycles.[25] Besides, PCMs are highly scalable[26] and can be simply deposited via sputtering onto any substrate without the "lattice mismatch" issue. Consequently, PCMs have already been used in compact, low-energy, and broadband programmable PICs for switches,[15,27–33] memories,[2,34] and computing.[35–38] However, scalable control over the states of PCMs for a chip-scale PIC system of a much higher complexity is yet to be resolved. Success in developing this technology will essentially enable highly scalable photonic switching units as critical building blocks for the future optical FPGAs.

Previously, reversible phase transitions of PCMs on PICs have been actuated by free-space optical heating, on-chip optical heating, or electrical threshold switching. Free-space optical heating[15,28,29] by far-field focused laser pulses is not viable for large-scale integration due to the slow, diffraction-limited, inaccurate alignment process.[15] On-chip optical heating,[2,20,21,30,32,34–38] assisted by evanescent coupling of near-field optical pulses from waveguides to PCMs, can support fully integrated all-optical operations but has difficulty in switching large-area PCMs and complex light routing,[37] leading to limited switching contrast and system complexity. Both optical heating approaches also suffer from the weak or non-existent photothermal effect of the relatively transparent amorphous state in the recrystallization process.[2,32,39,40] Whereas classical electrical threshold switching[21] allows large-scale integration, the limited phase transition volume due to the crystallization

filamentation[41] and nonuniform heating is not suitable for photonic applications. Recently, electrical switching with external heaters[31–33] has shown promising results in PCM-integrated photonics. However, in these demonstrations, a large insertion loss is incurred due to the use of indium tin oxide (ITO) heaters[31,32] or uniformly doped silicon heaters,[33] large driving voltages (>10 V) are applied, and the number of switching cycles is limited to ≈5–50. Here, we show that, by integrating GST on silicon PIN diode (p-type, intrinsic, n-type junction) heaters, it is feasible to reversibly trigger large-area phase transitions over more than 1000 times (500 cycles) under low voltages (down to 1 V for crystallization and 2.5 V for amorphization) with near-zero additional loss (≈0.02 dB μm^{-1}). Utilizing GST-on-silicon waveguides and microring resonators, we demonstrate CMOS-compatible, compact, and energy-efficient nonvolatile electrically reconfigurable photonic switching units that exhibit strong attenuation and optical phase modulation effects and are suitable for creating large-scale optical FPGAs.

As illustrated in **Figure 1**a, our photonic switching units were fabricated (see the Experimental Section) on a silicon-on-insulator (SOI) wafer with a 220-nm-thick silicon top layer. The partially etched silicon waveguide consists of a 500-nm-wide rib on a 100-nm-thick slab layer, supporting the propagation of single-mode transverse electric (TE) light. To form the PIN junction, the slab is heavily doped by boron and phosphorus ion implantation, 200 nm away from the left and right edge of the rib in the active region, respectively. The separation distance is close enough to the rib to reduce the resistance, but still far enough from the TE mode
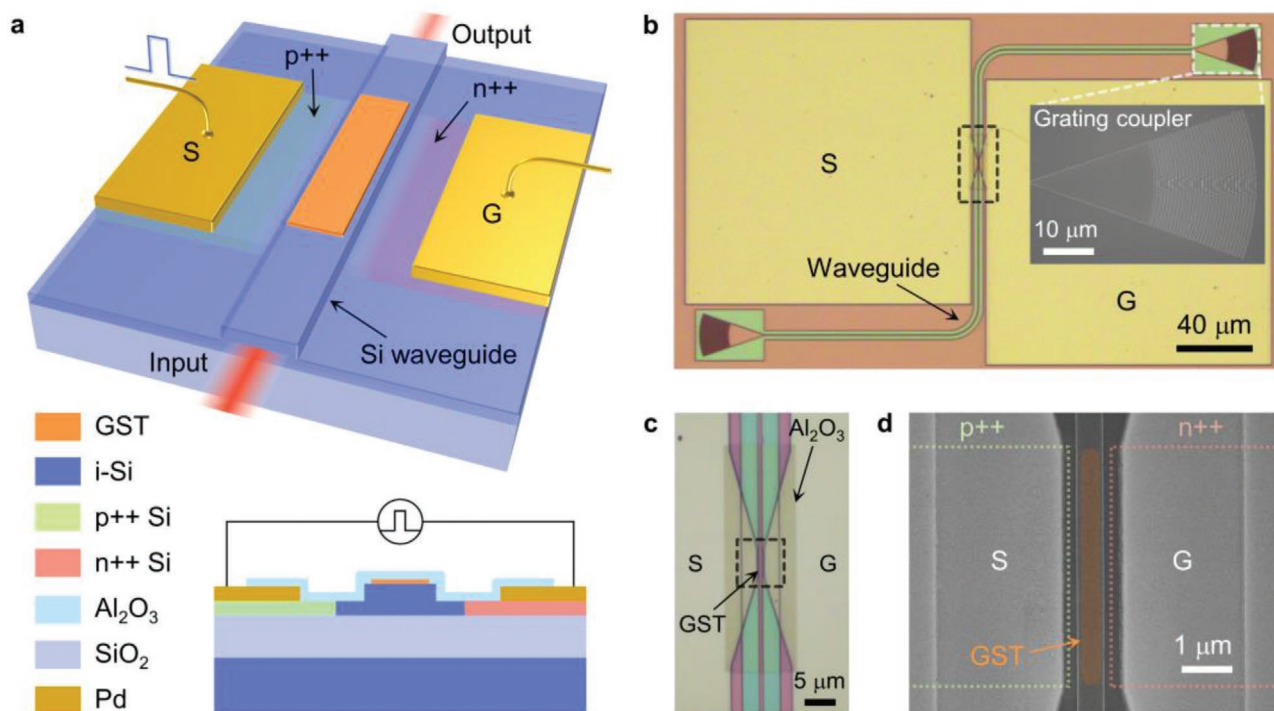

Figure 1. Nonvolatile electrically reconfigurable photonic switching units. a) Schematic of the device. For clarity, the top thin-film Al$_2$O$_3$ encapsulating layer is not displayed. Inset: cross-section of the device. b) Top-view optical microscope image of the switching unit on a waveguide with 10-nm-thick GST and a 5-μm-long active region. Inset: SEM image of the grating coupler. c) Optical microscope image of the black dashed area in (b). d) SEM image of the active region boxed in (c). False color is used to highlight the GST (orange). S (G), signal (ground) electrode. p++ (n++), heavily doped p (n)-type silicon region. i, intrinsic silicon region.

**ADVANCED
SCIENCE NEWS**

www.advancedsciencenews.com

**ADVANCED
MATERIALS**

www.advmat.de

distribution to ensure a negligible optical loss (see Section S2 in the Supporting Information for insertion loss analysis). The doping concentration is chosen as 10^{20} cm^{-3} to achieve high conductivity as well as Ohmic contact with the Ti/Pd (5 nm/180 nm) signal (S) and ground (G) electrodes for low-voltage operations. Pd is adopted because of its high-temperature tolerance. After metallization, a 10-nm or 20-nm thin-film of GST patch was sputtered onto the rib, inducing strong mode modification upon phase transitions through evanescent coupling. The GST and part of the electrodes near the heating region are encapsulated by 30-nm-thick Al$_2$O$_3$ through atomic layer deposition (ALD) (Figure 1a–c) to avoid oxidation and prevent the melted GST from reflowing and deforming during the amorphization process,[32] thus allowing high cyclability of the device. To obtain uniform heating and a large alignment tolerance in electron-beam lithography (EBL), the width and the length (in the direction of light propagation) of the GST patch are set to be smaller than those of the rib in the active region by 50 nm on each side (Figure 1a,d).

In contrast to optical heating and electrical threshold switching, phase transitions of our photonic switching units rely on the transfer of the electrical pulse-generated Joule heat from the in situ silicon waveguide PIN junctions. Hence, the switching region can be locally selected and be arbitrarily extended by increasing the size of the heaters, enabling large-scale integration and large-area functional devices such as directional couplers.[27] A 5-µm-long switching unit (i.e., the length of the GST patch is 4.9 µm) was operated here to demonstrate the transient response of the optical transmission and the simulated temperature distributions for the crystallization (Set) and amorphization (Reset) processes (see the Experimental Section). For the Set process (**Figure 2**a), we applied a single pulse of 3.5 V (≈10 mW) for 50 µs with a long falling edge of 30 µs (switching energy of ≈650 nJ, 12-ns rising edge for all the pulses in this paper) to ensure that the GST was heated to just above its glass transition temperature (T_g) but below the melting point (T_m) for a long enough time. The nucleation of
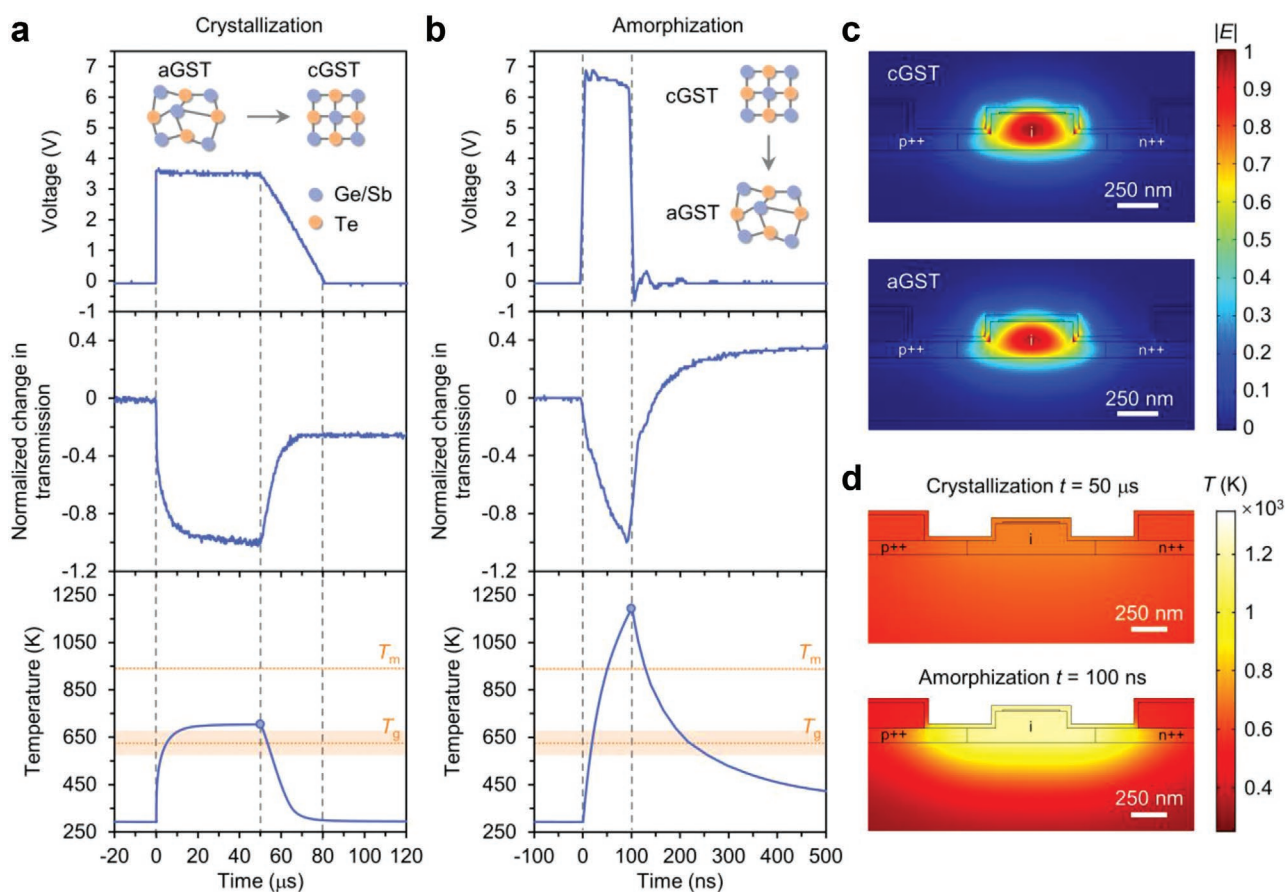

Figure 2. Operating principle of the photonic switching units. a,b) Real-time voltage of the applied electrical pulse (upper panel), corresponding change in optical transmission (with the minimum value normalized to −1) of the switching unit at 1550 nm (middle panel), and simulated temperature response in the center of the GST cross-section to the equivalent pulse with the same power and width (lower panel) for crystallization (Set, a) and amorphization (Reset, b). Insets of the upper panels: schematic of the GST structure changes due to the phase transitions. The orange shaded areas in the lower panel represent the assumed temperature intervals where the properties of GST are weighted sums of those in the amorphous and crystalline states during phase transitions. T_g, glass transition temperature of GST. T_m, melting point of GST. c) Simulated electric field (|E|) profiles for the fundamental quasi-TE mode of the switching unit at 1550 nm in the crystalline (top, $n_{eff} = 2.68–0.05i$) and amorphous (bottom, $n_{eff} = 2.60–1.06 \times 10^{-3}$ i) states. d) Simulated temperature (T) distributions of the switching unit cross-section for crystallization (top) and amorphization (bottom) at the time (t) marked by the dots in the lower panels of (a) and (b), respectively. aGST (cGST), amorphous (crystalline) GST. p++ (n++), heavily doped p (n)-type silicon region. i, intrinsic silicon region. Here, the length of the switching unit is 5 µm and the thickness of the GST is 10 nm.

small crystallites and subsequent growth can, therefore, proceed, leading to an elevated refractive index (n) and extinction coefficient (κ) of the GST (Section S4, Supporting Information) and a reduced optical transmission of the device after the pulse. For the Reset process (Figure 2b), a single pulse of 6.6 V (≈110 mW) for 100 ns (switching energy of ≈11 nJ) with a short falling edge of 12 ns (same for all the other Reset pulses) was utilized to melt the GST and then rapidly quench it below T_g, forming the disordered glass state with low optical constants and increased optical transmission of the device after the pulse. During the phase transitions, an ultrafast free-carrier absorption effect[42] due to the carrier injection into the silicon was observed from the steep change in the transmission at the sharp edges of the pulses. The slowly changed optical transmission at other times is, however, dominated by the thermo-optic effect of GST[43] in response to the heating and cooling processes. The overall switching period is then determined by the pulse width as well as the dead time due to the thermal relaxation (See Section S3 in the Supporting Information for heating dynamics analysis). Since the chip here was not ideally doped, the applied pulse voltages were higher than expected. This was improved in the following switching units on micro-ring resonators that were actuated by much lower driving voltages.

Strong mode modification is expected after the phase transitions according to the simulated mode profiles with amorphous and crystalline GST (see Figure 2c and the Experimental Section), implying substantial absorptive and refractive modulation effects of our switching units. As the mode distribution is mostly confined in the transparent intrinsic region, near-zero additional loss (≈0.02 dB µm⁻¹) is introduced by the PIN junction (Section S2, Supporting Information), showing promising scalability for optical FPGAs. To verify the phase transition processes, we further calculated (see the Experimental Section and Section S5 (Supporting Information)) the real-time optical transmission due to the effective index change based on the simulated carrier density and temperature distributions (Figure 2d), exhibiting good qualitative agreement with the experiment.

The Set process can also be actuated using current sweeps. **Figure 3**a presents the current–voltage (I–V) characteristic of a photonic switching unit on a waveguide during and after the Set by a current sweep, showing a typical rectification behavior of PIN junctions. In contrast to electrical threshold switching,[19] no abrupt change of the resistivity is observed in the I–V curves, confirming a different switching mechanism (i.e., electrical switching by external heaters) as the GST is not part of the electric circuit due to the relatively large resistance. The corresponding optical output under a current sweep
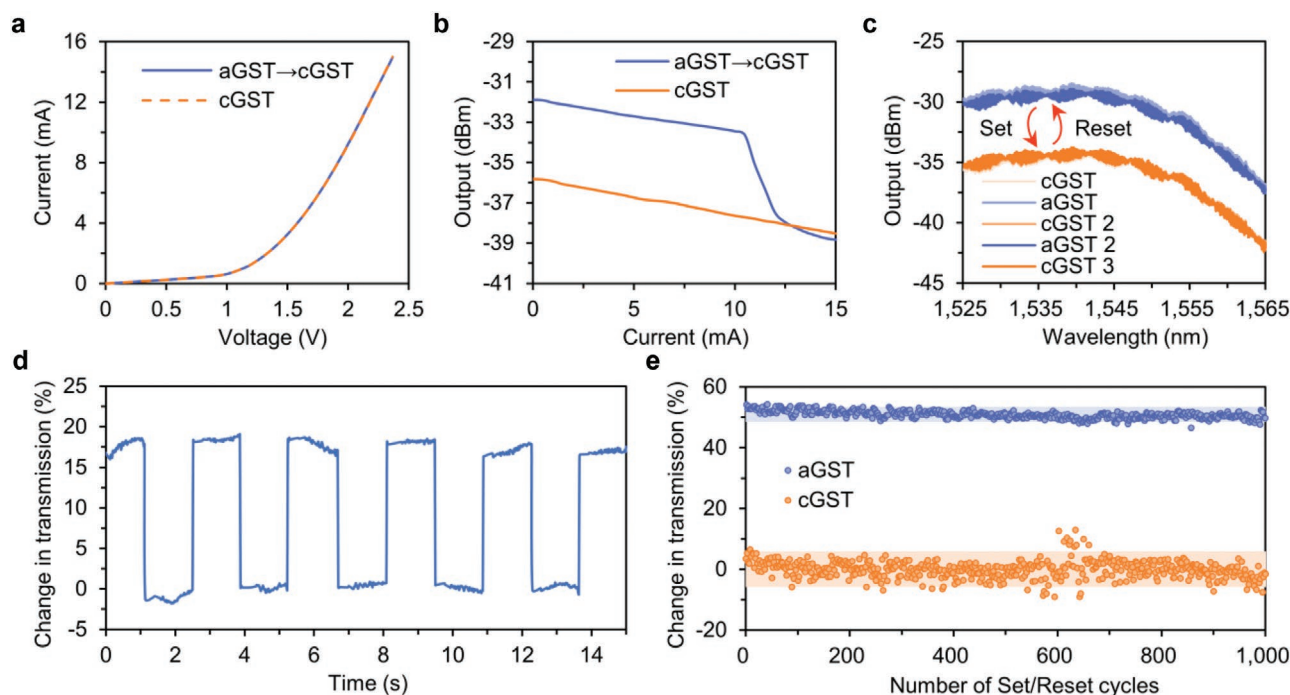

Figure 3. Performance of the photonic switching units on waveguides. a) Current–voltage (I–V) curves of the photonic switch with 20-nm-thick GST and a 4-µm-long active region obtained via current sweeps (0–15 mA) during and after the Set process, exhibiting a typical rectification behavior of PIN diodes without the electrical threshold switching effect. b) Corresponding optical output under current sweeps at 1550 nm, showing an abrupt change during the Set process. c) Optical output spectra of the same device after two reversible Set (0–15 mA sweep) and Reset (a single pulse of 4.3 V or ≈200 mW for 100 ns) processes. The periodic fringes in the spectra are due to the back reflection between the input and output grating couplers. d) Temporal trace of the transmission change in a photonic switch with 10-nm-thick GST and a 4-µm-long active region at 1550 nm during the consecutive Set (a single pulse of 3.4 V or ≈8 mW for 1 ms with a falling edge of 0.6 ms) and Reset (a single pulse of 7.1 V or ≈140 mW for 100 ns) steps. The sampling rate is ≈50 Hz. e) Cyclability of the transmission change of a photonic switch with 10-nm-thick GST and a 5-µm-long active region at 1550 nm under multiple Set (3.1 V or ≈11 mW for 50 µs, 30-µs falling edge, ≈715 nJ) and Reset (7 V or ≈130 mW for 100 ns, ≈13 nJ) cycles. Each pulse is temporally separated by more than 100 µs to ensure long enough thermal relaxation. The blue and orange shaded areas represent the two-standard-deviation intervals for the amorphous and crystalline states, respectively. aGST (cGST), amorphous (crystalline) GST.
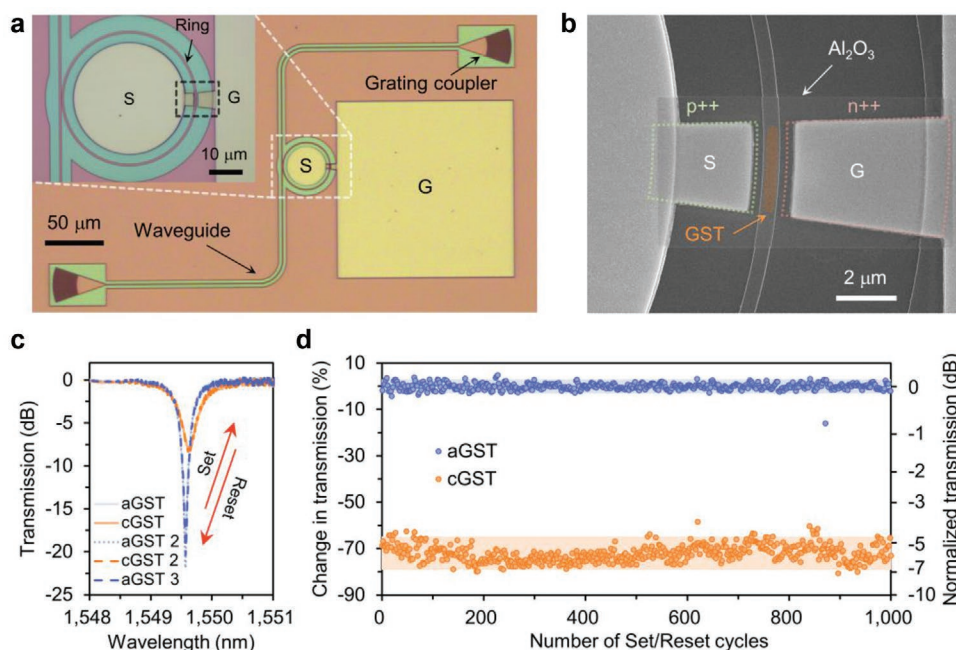
Figure 4. Photonic switching units on microring resonators. a) Top-view optical microscope image of the switching unit on an all-pass microring resonator. Inset: enlarged view of the ring. b) SEM image of the black dashed area in the inset of (a). False color is used to highlight the GST (orange). S (G), signal (ground) electrode. p++ (n++), heavily doped p (n)-type silicon region. c) Transmission spectra of a ring switch after a few reversible Set and Reset processes. d) Cyclability of the transmission change and normalized transmission of a ring switch at 1549.57 nm under multiple Set and Reset cycles. Each pulse is temporally separated by more than 0.1 s. The blue and orange shaded areas represent the two-standard-deviation intervals for the amorphous and crystalline states, respectively. Here, the radius of the rings is 20 μm, the gap between the rings and the bus waveguides is 240 nm, the length of the switching units is 3 μm, and the thickness of the GST is 10 nm. Set, a single pulse of 1 V or ≈0.6 mW for 100 μs with a falling edge of 60 μs, ≈78 nJ. Reset, a single pulse of 2.5 V or ≈80 mW for 100 ns, ≈8 nJ. aGST (cGST), amorphous (crystalline) GST.

(Figure 3b), however, does exhibit an obvious change due to the phase transition. Additionally, we find a transient gradual reduction of the output during the current sweep that can be again attributed to the carrier-injection induced loss from silicon and the thermo-optic effect of GST. Manually applying a current sweep (0–15 mA) and a Reset pulse (a single pulse of 4.3 V for 100 ns) shows that the device can be reversibly switched with a high extinction ratio of ≈5 dB (1.25 dB μm⁻¹ for 20-nm-thick GST) over a broad spectral range (Figure 3c). It is notable that although the energy consumption of one switching cycle may be larger compared with electro-optic switches or comparable with thermo-optic switches, due to the nonvolatility of GST, the output states are self-held, precluding any need for external control after the phase transitions. This nonvolatility leads to highly energy-efficient operations.

To further inspect the state retention and the cyclability of the switching units on waveguides, we applied numerous Set and Reset pulses and recorded the temporal trace (Figure 3d) and static states (Figure 3e) of the transmission change. The results show that our devices allow stable binary operations with reversible phase transitions over more than 1000 times. No obvious performance degradation was found after repeating the same experiment (1000 transitions) for several times, implying that a significantly longer endurance can be expected. The transmission fluctuation in Figure 3d is primarily caused by the gradual misalignment of the setup (see the Experimental Section and Section S1 (Supporting Information)) during the measurement while a relatively large uncertainty of the transmission

in the crystalline state (Figure 3e) can be explained due to partial crystallization of the GST.

By integrating the photonic switching units on microring resonators (**Figure 4**a,b), we can achieve even higher optical contrast from such a compact structure by taking the advantages of both the strong attenuation and optical phase modulation effects of GST at the cost of less switching energy. Figure 4c shows the transmission spectra of a microring resonator with a radius of 20 μm integrated with a 3-μm-long switching unit covered with 10-nm-thick GST. After several Set and Reset cycles, the spectra remain the same, indicating reversible phase transitions. Thanks to the better doping-induced electrical conductivity in this chip, much lower driving voltages for Set (1 V) and Reset (2.5 V) were required in this experiment. As a result of the combined effects of the resonance shift (≈0.02 nm μm⁻¹ switching unit length) and resonance dip (linewidth and depth) change due to the loss modulation (≈0.25 dB μm⁻¹ switching unit length) upon phase transitions (see Section S2 in the Supporting Information for resonance wavelength and loss extraction), a high on-off extinction ratio up to 14.7 dB was achieved near the resonance wavelength while the total switching energy of a cycle is only ≈86 nJ much less than that for the photonic switching units on waveguides with the same GST area or the same switching contrast. High cyclability with over more than 1000 phase transitions was also realized (Figure 4d) in a ring-based switch with the same structure. Note that due to a slight shift between the probe laser wavelength and the ring resonance, the extinction ratio here is not optimal. The relatively

**ADVANCED
SCIENCE NEWS**
www.advancedsciencenews.com

**ADVANCED
MATERIALS**
www.advmat.de

large uncertainty of the transmission in the crystalline state can be attributed to the thermal shift of the resonant wavelength and partial crystallization.

In summary, we have demonstrated nonvolatile electrically reconfigurable PCM-integrated photonic switches with near-zero additional insertion loss ($\approx$0.02 dB μm^{-1}) and high endurance (>1000 transitions) using in situ silicon waveguide PIN heaters. By leveraging the remarkable broadband attenuation and optical phase modulation of GST, high extinction ratios are obtained in small footprints (1.25 dB μm^{-1} for waveguides and $\approx$15 dB for a microring with a 3-μm-long switching unit) under low driving voltages (down to 1 V for Set and 2.5 V for Reset). The static (nonvolatile) nature of the modulation ensures intrinsically high energy-efficiency. We expect that the extinction ratio can be further improved by carefully choosing the power of the applied pulses to achieve complete phase transitions or simply increase the length of the switching units. Multi-level operations can be potentially achieved when the intermediate states are reached via engineering pulse shape, power, and duration.[2,15,32–38] The insertion loss of the devices can be reduced through thinner electrodes and improved fabrication (Section S2, Supporting Information) as well as emerging wide-bandgap PCMs.[39,40] Moreover, the speed of the devices (reported in our paper $\approx$10 kHz) can be enhanced to as fast as $\approx$4 MHz by optimally increasing the pulse power to reduce the pulse width and dead time without inducing reamorphization or ablation.[44] However, the error tolerance in setting the electrical power decreases with the increase of the pulse power and a better-controlled environment will be needed to avoid any damage to the GST. To realize multi-port and broadband photonic switches, our photonic switching units can be integrated on the recently reported three-waveguide directional coupler structure.[27] The devices can also be similarly applied to more commonly used SiO_2-clad silicon PICs without losing their high performance.[44] With low-energy, compact, low-loss, low-voltage, and high-cyclability operations at moderate speeds as well as the easy-to-deposit property of PCMs and the mature CMOS technology for silicon PIN diodes, our static photonic switching units promise large-scale integration of programmable PICs and pave the way for CMOS-integrated programmable electronic–photonic systems such as optical neural networks and optical FPGAs.

Experimental Section

Device Fabrication: The photonic switches were fabricated on a commercial SOI wafer with a 220-nm-thick silicon layer on top of a 3-μm-thick buried oxide. The rib waveguides, microring resonators, and grating couplers (with a pitch of 744 nm and a duty cycle of 0.5, inset of Figure 1b) were defined by EBL (JEOL JBX-6300FS) using positive tone resist (ZEP-520A) and etched by inductively coupled plasma reactive ion etching (ICP-RIE, Oxford PlasmaLab 100 ICP-180) exploiting mixed gas of SF_6 and C_4F_8. The p++ (n++) regions were defined by another EBL using 600-nm-thick poly(methyl methacrylate) (PMMA) resist and implanted by boron (phosphorus) ions with a dosage of 2×10^{15} ions per cm^2 and ion energy of 14 keV (40 keV). The ion implantation was conducted at a tilt angle of 7° to misalign with the silicon lattice and thus achieve uniform deep doping. Subsequently, the chips were annealed at 950 °C for 10 min to activate the dopants. Before metallization, the surface native oxide was removed by immersing the chips in 10:1 buffered oxide etchant (BOE) for 10 s to ensure Ohmic contact. The metal contacts

were then immediately patterned by the fourth EBL using PMMA and formed by electron-beam evaporation (CHA SEC-600) and lift-off of Ti/Pd (5 nm/180 nm) layers. After patterning the windows for the GST by EBL with PMMA, 10-nm or 20-nm GST was deposited onto the chips using a GST target (AJA International) in a magnetron sputtering system (Lesker Lab 18) followed by a lift-off process. The GST and part of the electrodes close to the heating region were then encapsulated by 30-nm-thick Al_2O_3 through EBL patterning with PMMA, ALD (Oxford Plasmalab 80PLUS OpAL ALD) at 100 °C, and lift-off. Finally, rapid thermal annealing (RTA) at 200 °C for 10 min was performed to ensure the complete crystallization of the GST.

Experimental Setup and Static Measurement: The photonic switches were characterized by a vertical fiber-coupling setup (Section S1, Supporting Information). All the measurements were performed under ambient conditions while the temperature of the stage was fixed at $\approx$22 °C by a thermoelectric controller (TEC, TE Technology TC-720) to prohibit the serious thermal shift of the resonators. The input light was provided by a tunable continuous-wave laser (Santec TSL-510) and its polarization was controlled by a manual fiber polarization controller (Thorlabs FPC526) to match the fundamental quasi-TE mode of the waveguides. Focusing grating couplers optimized for $\approx$1550 nm were employed to couple light into and out of the devices operated at an angle of $\approx$25°. The power of the coupled light was kept to be sufficiently low (< 100 μW) in order to minimize the thermo-optic effects of GST[43] and silicon[45] and avoid causing any phase transition. A low-noise power meter (Keysight 81634B) was used to collect the static optical output from the grating couplers. Based on this setup, the transmission spectrum measurement was performed after each important fabrication step for all the devices including the reference devices without any doping, metal, or GST to assist the insertion loss analysis (Section S2, Supporting Information) and normalization. To measure the *I–V* characteristic and conduct electrical switching, electrical signals were applied to the contacts by a pair of DC probes controlled by two probe positioners (Cascade Microtech DPP105-M-AI-S). In particular, the current sweep and voltage measurement were provided by a source meter (Keithley 2450) and the Set and Reset pulses were generated from a pulse function arbitrary generator (Keysight 81160A). The measured *I–V* curves were used to estimate the power of the applied pulses. By comparing the pulses directly from the pulse generator and those from the probes via a fast oscilloscope (Agilent DSO1022A), no signal distortion was found, suggesting that the probe system has enough response speed for the experiment. Limited by the low control speed of the pulse generator (each pulse takes over 0.1 s), cyclability operations with a higher order of magnitude will take hours and thus were not conducted since the setup would have got badly misaligned within such long time.

Transient Response Measurement: To obtain the time-resolved response of the photonic switches under the electrical pulses, high-speed low-noise photoreceivers (New Focus 1811 and 1611) were used to measure the dynamic optical signals and the converted output electrical signals were recorded using the oscilloscope triggered by the applied pulses from the pulse generator (see Section S1 in the Supporting Information for the setup). The 125-MHz photoreceiver (New Focus 1811) has enough response speed and appropriate linear operation region to analyze the phase transitions (Figure 2a,b), pulse amplitude modulation (PAM) effects, and transient response of the rings at different wavelengths (Section S3, Supporting Information). However, for the analysis of pulse width modulation (PWM) effects, the 1-GHz photoreceiver (New Focus 1611) was necessary. Since its linear operation power was $\approx$1 mW, the output light from grating couplers was first amplified by an optical fiber amplifier (Amonics AEDFA-30-B-FA) and filtered by a narrow-band optical demultiplexer (DEMUX, JDS WD1504D4A-DSC4). The power of the amplified light was then attenuated by a variable optical attenuator (Keysight 81570A) to meet the requirement of linear operation. In this experiment, the wavelength of the input light was fixed at 1549.32 nm in corresponding to the nominal central wavelength of the second channel of the DEMUX.

Device Modeling and Simulation: A coupled electro-thermal 2D finite-element method (FEM) model was developed using COMSOL Multiphysics to qualitatively simulate the electrical switching of the photonic devices with PIN heaters. In the simulation, a semiconductor

module (Semiconductor Interface) based on the Poisson's equation, current continuity equation, and drift-diffusion current density equations[46] was utilized to predict the electric potential, current density, and carrier density distributions in the PIN junctions. A heat transfer module (Heat Transfer in Solids Interface) based on the heat transfer equation $\rho C_p \frac{dT}{dt} = \nabla \cdot (k_{th} \nabla T) + Q_e$ (where ρ is the material density, C_p is the specific heat, k_{th} is the thermal conductivity, and Q_e is the heat source) was exploited to predict the temperature distributions of the whole switching units. The two modules were cross-coupled via the temperature-dependent material parameters (Section S4, Supporting Information) and the total heat calculated from the semiconductor module including Joule heating and nonradiative recombination heating. The schematic of the model was consistent with the actual device cross-section except that the dopants here were assumed to be uniformly distributed for the sake of simplicity.

In the semiconductor module, the Fermi-Dirac carrier statistics and Jain-Roulston bandgap narrowing model were applied due to the high doping level. The Arora mobility model was used to simulate the effect of phonon/lattice and impurity scattering while the Fletcher mobility model was added to describe the carrier-carrier scattering at high voltage. Trap-assisted recombination and Auger recombination for high bias were also considered in the module. The metal contacts were assumed to be ideal Ohmic and the applied pulses had ideal shapes. All the other external boundaries were electrically insulated.

In the heat transfer module, the infinite element domains were adopted for the left, right, and bottom boundary regions of the model while the convective heat flux boundary condition was used on the surface with a heat transfer coefficient of 5 W m^{-2} K^{-1}. Considering the relative thinness of GST and high operating temperature, thermal boundary resistance (TBR) and surface-to-surface radiation boundaries were utilized. For simplicity without losing generality, the phase transition processes were phenomenologically modeled as that the material properties of GST were weighted sums of those in the amorphous and crystalline states in a small temperature interval $\Delta T_m = 10$ K ($\Delta T_g = 100$ K) centered at $T_m = 888$ K ($T_g = 673$ K) of GST for melting (quenching and crystallization) with latent heat of 66.81 kJ kg^{-1} (exothermic heat of 37.22 kJ kg^{-1}) involved.[41] Note that T_g was set to be higher than usual (≈ 423 K) due to the increased T_g at a high heating rate.[47]

The mode profiles of the photonic switching units were also modeled based on the same geometry but simulated using a frequency-domain 2D FEM wave optics model through the mode analysis (eigenvalue solver). The carrier density and temperature distributions calculated from the electro-thermal model were employed to determine the complex refractive index of the materials (Section S4, Supporting Information) during the Set and Reset processes. The transmission of the switching units was then estimated based on the solved effective indices (Section S5, Supporting Information), qualitatively agreeing with the transient response obtained in the experiment. The discrepancy in specific values was attributed to the simple model of the phase transitions model as well as the uncertainty in the material properties and volume of GST phase transitions. More sophisticated simulations can be conducted by including the kinetic models of melting, vitrification, nucleation, and growth[41] and applying accurate material parameters obtained by material characterizations in the future.

Supporting Information

Supporting Information is available from the Wiley Online Library or from the author.

Acknowledgements

Conflict of Interest

The authors declare no conflict of interest.

Author Contributions

J.Z., J.K.D., and A.M. conceived the project. J.Z. simulated, designed, and fabricated the devices. J.Z. performed the experiments. Z.F. helped with the reversible switching of PCMs. C.W. and M.L. helped with the transient response measurement. S.Z. and S.D. (University of Washington) conducted the annealing simulation and thermal conductivity modeling. P.X. helped with the transmission measurement. S.D. (Stanford University) and E.P. helped with GST deposition and process characterization to increase the endurance. A.M. supervised the overall progress of the project. J.Z. wrote the manuscript with input from all the authors.

Keywords

[1] A. H. Atabaki, S. Moazeni, F. Pavanello, H. Gevorgyan, J. Notaros, L. Alloatti, M. T. Wade, C. Sun, S. A. Kruger, H. Y. Meng, K. Al Qubaisi, I. Wang, B. H. Zhang, A. Khilo, C. V. Baiocco, M. A. Popovic, V. M. Stojanovic, R. J. Ram, *Nature* **2018**, *556*, 349.

[2] C. Rios, M. Stegmaier, P. Hosseini, D. Wang, T. Scherer, C. D. Wright, H. Bhaskaran, W. H. P. Pernice, *Nat. Photonics* **2015**, *9*, 725.

[3] Y. Shen, N. C. Harris, S. Skirlo, M. Prabhu, T. Baehr-Jones, M. Hochberg, X. Sun, S. J. Zhao, H. Larochelle, D. Englund, M. Soljacic, *Nat. Photonics* **2017**, *11*, 441.

[4] N. C. Harris, G. R. Steinbrecher, M. Prabhu, Y. Lahini, J. Mower, D. Bunandar, C. C. Chen, F. N. C. Wong, T. Baehr-Jones, M. Hochberg, S. Lloyd, D. Englund, *Nat. Photonics* **2017**, *11*, 447.

[5] J. Wang, S. Paesani, Y. H. Ding, R. Santagati, P. Skrzypczyk, A. Salavrakos, J. Tura, R. Augusiak, L. Mancinska, D. Bacco, D. Bonneau, J. W. Silverstone, Q. H. Gong, A. Acin, K. Rottwitt, L. K. Oxenlowe, J. L. O'Brien, A. Laing, M. G. Thompson, *Science* **2018**, *360*, 285.

**ADVANCED
SCIENCE NEWS**

www.advancedsciencenews.com

**ADVANCED
MATERIALS**

www.advmat.de

[6] L. Zhuang, C. G. H. Roeloffzen, M. Hoekman, K. J. Boller, A. J. Lowery, *Optica* **2015**, *2*, 854.

[7] W. Liu, M. Li, R. S. Guzzon, E. J. Norberg, J. S. Parker, M. Z. Lu, L. A. Coldren, J. P. Yao, *Nat. Photonics* **2016**, *10*, 190.

[8] D. Perez, I. Gasulla, L. Crudgington, D. J. Thomson, A. Z. Khokhar, K. Li, W. Cao, G. Z. Mashanovich, J. Capmany, *Nat. Commun.* **2017**, *8*, 636.

[9] N. C. Harris, J. Carolan, D. Bunandar, M. Prabhu, M. Hochberg, T. Baehr-Jones, M. L. Fanto, A. M. Smith, C. C. Tison, P. M. Alsing, D. Englund, *Optica* **2018**, *5*, 1623.

[10] D. Perez, I. Gasulla, J. Capmany, *Nanophotonics* **2018**, *7*, 1351.

[11] S. Chen, Y. Shi, S. He, D. Dai, *Opt. Lett.* **2016**, *41*, 836.

[12] L. Lu, S. Y. Zhao, L. J. Zhou, D. Li, Z. X. Li, M. J. Wang, X. W. Li, J. P. Chen, *Opt. Express* **2016**, *24*, 9295.

[13] L. Qiao, W. Tang, T. Chu, *Sci. Rep.* **2017**, *7*, 42306.

[14] M. Wuttig, H. Bhaskaran, T. Taubner, *Nat. Photonics* **2017**, *11*, 465.

[15] J. Zheng, A. Khanolkar, P. Xu, S. Deshmukh, J. Myers, J. Frantz, E. Pop, J. Hendrickson, J. Doylend, N. Boechler, A. Majumdar, *Opt. Mater. Express* **2018**, *8*, 1551.

[16] M. Wuttig, N. Yamada, *Nat. Mater.* **2007**, *6*, 824.

[17] K. Shportko, S. Kremers, M. Woda, D. Lencer, J. Robertson, M. Wuttig, *Nat. Mater.* **2008**, *7*, 653.

[18] H. S. P. Wong, S. Raoux, S. Kim, J. L. Liang, J. P. Reifenberg, B. Rajendran, M. Asheghi, K. E. Goodson, *Proc. IEEE* **2010**, *98*, 2201.

[19] F. Xiong, A. D. Liao, D. Estrada, E. Pop, *Science* **2011**, *332*, 568.

[20] J. von Keitz, J. Feldmann, N. Gruhler, C. Rios, C. D. Wright, H. Bhaskaran, W. H. P. Pemice, *ACS Photonics* **2018**, *5*, 4644.

[21] N. Farmakidis, N. Youngblood, X. Li, J. Tan, J. L. Swett, Z. Cheng, C. D. Wright, W. H. P. Pernice, H. Bhaskaran, *Sci. Adv.* **2019**, *5*, eaaw2687.

[22] S. Raoux, M. Wuttig, *Phase Change Materials: Science and Applications*, Springer, New York **2009**.

[23] D. Loke, T. H. Lee, W. J. Wang, L. P. Shi, R. Zhao, Y. C. Yeo, T. C. Chong, S. R. Elliott, *Science* **2012**, *336*, 1566.

[24] F. Rao, K. Y. Ding, Y. X. Zhou, Y. H. Zheng, M. J. Xia, S. L. Lv, Z. T. Song, S. L. Feng, I. Ronneberger, R. Mazzarello, W. Zhang, E. Ma, *Science* **2017**, *358*, 1423.

[25] S. Raoux, F. Xiong, M. Wuttig, E. Pop, *MRS Bull.* **2014**, *39*, 703.

[26] S. Raoux, G. W. Burr, M. J. Breitwisch, C. T. Rettner, Y. C. Chen, R. M. Shelby, M. Salinga, D. Krebs, S. H. Chen, H. L. Lung, C. H. Lam, *IBM J. Res. Dev.* **2008**, *52*, 465.

[27] P. Xu, J. Zheng, J. K. Doylend, A. Majumdar, *ACS Photonics* **2019**, *6*, 553.

[28] D. Tanaka, Y. Shoji, M. Kuwahara, X. M. Wang, K. Kintaka, H. Kawashima, T. Toyosaki, Y. Ikuma, H. Tsuda, *Opt. Express* **2012**, *20*, 10283.

[29] M. Rude, J. Pello, R. E. Simpson, J. Osmond, G. Roelkens, J. J. G. M. van der Tol, V. Pruneri, *Appl. Phys. Lett.* **2013**, *103*.

[30] M. Stegmaier, C. Rios, H. Bhaskaran, C. D. Wright, W. H. P. Pernice, *Adv. Opt. Mater.* **2017**, *5*, 1600346.

[31] K. Kato, M. Kuwahara, H. Kawashima, T. Tsuruoka, H. Tsuda, *Appl. Phys. Express* **2017**, *10*, 072201.

[32] C. M. Wu, H. S. Yu, H. Li, X. H. Zhang, I. Takeuchi, M. Li, *ACS Photonics* **2019**, *6*, 87.

[33] H. Zhang, L. J. Zhou, L. J. Lu, J. Xu, N. N. Wang, H. Hu, B. M. A. Rahman, Z. P. Zhou, J. P. Ghen, *ACS Photonics* **2019**, *6*, 2205.

[34] X. Li, N. Youngblood, C. Rios, Z. G. Cheng, C. D. Wright, W. H. P. Pernice, H. Bhaskaran, *Optica* **2019**, *6*, 1.

[35] J. Feldmann, N. Youngblood, C. D. Wright, H. Bhaskaran, W. H. P. Pernice, *Nature* **2019**, *569*, 208.

[36] Z. Cheng, C. Ríos, W. H. P. Pernice, C. D. Wright, H. Bhaskaran, *Sci. Adv.* **2017**, *3*, 1700160.

[37] J. Feldmann, M. Stegmaier, N. Gruhler, C. Rios, H. Bhaskaran, C. D. Wright, W. H. P. Pernice, *Nat. Commun.* **2017**, *8*, 1256.

[38] C. Ríos, N. Youngblood, Z. Cheng, M. Le Gallo, W. H. Pernice, C. D. Wright, A. Sebastian, H. Bhaskaran, *Sci. Adv.* **2019**, *5*, eaau5759.

[39] W. Dong, H. Liu, J. K. Behera, L. Lu, R. J. Ng, K. V. Sreekanth, X. Zhou, J. K. Yang, R. E. Simpson, *Adv. Funct. Mater.* **2018**, 1806181.

[40] Y. Zhang, J. B. Chou, J. Li, H. Li, Q. Du, A. Yadav, S. Zhou, M. Y. Shalaginov, Z. Fang, H. Zhong, C. Roberts, P. Robinson, B. Bohlin, C. Rios, H. Lin, M. Kang, T. Gu, J. Warner, V. Liberman, K. Richardson, J. Hu, *Nat. Commun.* **2019**, *10*, 4279.

[41] A. Redaelli, A. Pirovano, A. Benvenuti, A. L. Lacaita, *J. Appl. Phys.* **2008**, *103*, 111101.

[42] G. T. Reed, G. Mashanovich, F. Y. Gardes, D. J. Thomson, *Nat. Photonics* **2010**, *4*, 518.

[43] M. Stegmaier, C. Rios, H. Bhaskaran, W. H. P. Pernice, *ACS Photonics* **2016**, *3*, 828.

[44] J. Zheng, S. Zhu, P. Xu, S. Dunham, A. Majumdar, *ACS Appl. Mater. Interfaces* **2020**, *12*, 21827.

[45] V. R. Almeida, M. Lipson, *Opt Lett.* **2004**, *29*, 2387.

[46] S. M. Sze, K. K. Ng, *Physics of Semiconductor Devices*, John Wiley & Sons, Hoboken **2006**.

[47] J. Orava, A. L. Greer, B. Gholipour, D. W. Hewak, C. E. Smith, *Nat. Mater.* **2012**, *11*, 279.

2001218 (8 of 8)